V. S. N. Ranjith Kumar
Institute Center for Energy (iEnergy),
Department of Mechanical and
Materials Engineering,
Masdar Institute of Science and Technology,
P.O. Box 54224,
Abu Dhabi ■, UAE

S. Kumar[1]
Mem. ASME
Institute Center for Energy (iEnergy),
Department of Mechanical and
Materials Engineering,
Masdar Institute of Science and Technology,
P.O. Box 54224,
Abu Dhabi ■, UAE
e-mails: kshanmugam@masdar.ac.ae;
s.kumar@eng.oxon.org

G. Pal[2]
Institute Center for Energy (iEnergy),
Department of Mechanical and
Materials Engineering,
Masdar Institute of Science and Technology,
P.O. Box 54224,
Abu Dhabi ■, UAE

Tushar Shah
Applied Nanostructured Solutions,
LLC, 2323 Eastern Boulevard MP 50,
Baltimore ■, MD

High-Ampacity Overhead Power Lines With Carbon Nanostructure–Epoxy Composites

Design of high-performance power lines with advanced materials is indispensable to effectively eliminate losses in electrical power transmission and distribution (T&D) lines. In this study, aluminum conductor composite core with carbon nanostructure (ACCC–CNS) coating in a multilayered architecture is considered as a novel design alternative to conventional aluminum conductor steel-reinforced (ACSR) transmission line. In the multiphysics approach presented herein, first, electrothermal finite element (FE) analysis of the ACSR line is performed to obtain its steady-state temperature for a given current. Subsequently, the sag distance of the ACSR line due to self-weight and thermal expansion is determined by performing thermostructural analysis employing an analytical model. The results are then verified with those obtained from the FE analysis of the ACSR line. The electrothermal FE model and the thermostructural analytical model are then extended to the ACCC–CNS line. The results indicate that the ACCC–CNS line has higher current-carrying capacity (CCC) and lower sag compared to those of the ACSR line. Motivated by the improved performance of the ACCC–CNS line, a systematic parametric study is conducted in order to determine the optimum ampacity, core diameter, and span length. The findings of this study would provide insights into the optimal design of high-performance overhead power lines. [DOI: 10.1115/1.4034095]

Keywords: overhead power lines, electrothermal analysis, thermostructural analysis, sag, ampacity, carbon nanostructure–epoxy composites

1 Introduction

Design of high-performance power lines with advanced materials is indispensable to effectively eliminate losses in electrical power T&D lines. Carbon nanotubes (CNTs) reinforced polymer composites are attractive to engineers due to their excellent thermal, mechanical, and electrical properties [1–3]. Application-specific properties can be optimized by tailoring the alignment and distribution of CNS (bundles of aligned CNTs) in the polymer matrix. CNS material used in this research is fabricated by one of the authors at Applied Nanostructured Solutions, Baltimore, MD. These materials with tailored properties can reduce line losses because of their improved specific properties. This motivated us to use CNS/epoxy composite material for power transmission lines in a multilayered architecture to minimize the transmission losses. Transmission losses in overhead power lines occur due to resistive Joule heating, dielectric heating, corona discharge, etc. Among these, loss due to resistive Joule heating is the major energy loss as it is associated with inherent electrical resistivity of the conductor. Copper was the first metal used for the electric transmission owing to its higher electrical conductivity. Subsequently, aluminum began to replace copper because of its high specific electrical conductivity ("specific": normalized by the linear mass density) and low cost, although it has moderate electrical conductivity. However, its higher coefficient of linear thermal expansion (CTE) results in higher line sag. In order to minimize the sag of all aluminum conductor lines, ACSR line was introduced as the steel core provides extra strength and resistance to sag [4]. ACSR lines were subsequently improvised by aluminum conductor alumoweld steel-reinforced (ACSR/AW) line to avoid galvanic corrosion of steel strands [4].

Composite materials are more attractive than the traditional materials (metals) for T&D of electricity due to their superior specific properties. Electrical equipment manufacturers such as 3M and CTC Global have developed new transmission lines as alternatives to conventional ACSR line [5–7]. 3M has developed aluminum conductor composite-reinforced (ACCR) line in which the steel core of the wire is replaced by metal matrix composite. Similarly, CTC Global has developed ACCC line in which steel strands of conventional ACSR line are replaced by a hybrid core of glass/carbon fiber-reinforced polymer matrix composite. Surface coated hybrid glass/carbon epoxy composite core was found to significantly reduce thermal aging and retain flexural stiffness and strength [8–11]. In this current study, a multilayered architecture composed of CNS/epoxy composite, glass fiber-reinforced composite (GFRC) core, and aluminum conductor is proposed as an alternative to ACSR line, and its performance is evaluated both computationally and analytically (Fig. 1).

Many researchers [12–20] have developed analytical and numerical methods for multiphysics analysis of transmission lines. In the current study, coupled electrical–thermal and coupled thermal–structural analyses are performed sequentially to determine the performance of the power lines. Both computational and analytical models are developed to show that the ACCC–CNS line is superior to an equivalent ACSR line. Using the developed analytical model, parametric studies were

[1]Corresponding author.

[2]Present address: ■, Amity University, Uttar Pradesh ■, India.

Contributed by the Materials Division of ASME for publication in the Journal of Engineering Materials and Technology. Manuscript received September 6, 2015; final manuscript received June 27, 2016; published online xx xx, xxxx. Assoc. Editor: Harley Johnson.

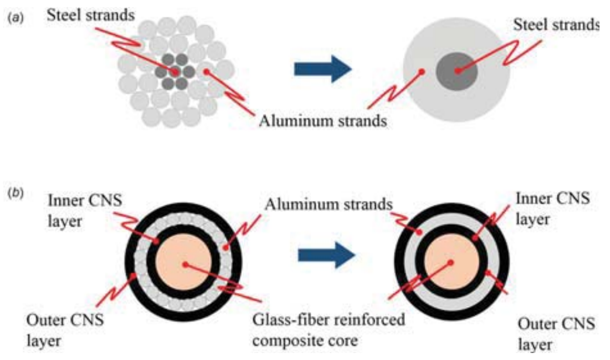

Fig. 1 Schematic diagram representing the cross-sectional details of stranded and equivalent cylindrical cross sections: (*a*) ACSR line and (*b*) ACCC–CNS lines

performed for the proposed ACCC–CNS line by combining the coupled electrical–thermal and coupled thermal–structural analyses to determine improved ampacity, percentage reduction in core diameter, and/or percentage increase in span length. The paper is organized as follows: Section 2 contains the details of the fabrication and properties of CNS and CNS/epoxy composites. Section 3 describes the multiphysics modeling approaches used for determining the operating temperature and the sag of ACCC–CNS lines. Section 4 presents the results of electrothermal and thermostructural analyses with relevant discussion. Finally, Sec. 5 contains the conclusions of the research work presented in this study.

2 Material Characterization

CNS is a new form of nanomaterial, containing clusters of highly aligned multiwall CNTs. The CNS is grown on glass fibers substrate through plasma-enhanced chemical vapor deposition process [21,22]. The glass substrate used for CNS growth can be of various shapes and formations such as spoolable glass fiber tows, glass tapes, woven glass fabric, and glass fiber mats. In the first step, glass fibers (or woven fabric) are treated with a plasma etching process in order to facilitate surface bonding of the catalyst and the CNS to substrate glass fibers. The etched glass fibers are then immersed into the aqueous solution of hydrogen peroxide, ferrous acetate, and cobalt acetate. The deposited ferrous and cobalt salts work as the precursor catalyst for CNT growth. Following the deposition, the glass fibers are heated to 300–450 °C to convert catalyst precursors into intermediate catalyst (γ-Fe_3O_4 (maghemite), α-Fe_3O_4 (hematite), cobalt ferrite ($CoFe_2O_4$), and cobaltous oxide (CoO)). The heated fibers are further heated up to 550–800 °C in the presence of acetylene or ethylene gas. At 700 °C, pyrolysis of acetylene (or ethylene) takes place and hydrogen gas and atomic carbon are released [22]. At this temperature, hydrogen gas reduces the intermediate catalysts in active transitional metal carbide nanoparticles, and the presence of atomic carbon with metal catalytic particles results in the formation and growth of CNTs forest on the substrate glass fibers. In the last step, these bundles of CNTs are removed from glass fibers in the form of CNS material. Figure 2 shows the high-resolution scanning electron micrograph (SEM) of CNS materials. High degree of CNT alignment offers improved physical and transport properties to CNS material as compared to those of randomly crosslinked CNT clusters. This presents a unique opportunity to develop high-performance ACCC–CNS power lines with improved heat dissipation capabilities.

The proposed multilayered architecture of ACCC–CNS line comprises four concentric layers, namely, central GFRC core, inner-CNS composite layer, aluminum conductor layer, and outer-CNS composite layer (see Fig. 1). The GFRC core composed of 60 wt.% glass fibers carries the thermomechanical load of the line and controls the line sag. The CNS content in CNS/epoxy coating is approximately 3–4% by weight. The inner-CNS layer protects the composite core from stray radio frequency genetared by the electromagnetic pulse emanating from high electric current-carrying aluminum conductor. The outer-CNS layer absorbs the heat generated in the aluminum conductor layer and dissipates it to the surrounding atmosphere through convection and radiation. It further protects the conducting aluminum strands from external damage such as lightning strike and foreign object impact. Moreover, it enables de-icing capability [23].

Extensive characterization and experimental tests were conducted to evaluate the electrical, thermal, and mechanical properties of CNS material and CNS/epoxy composites. The

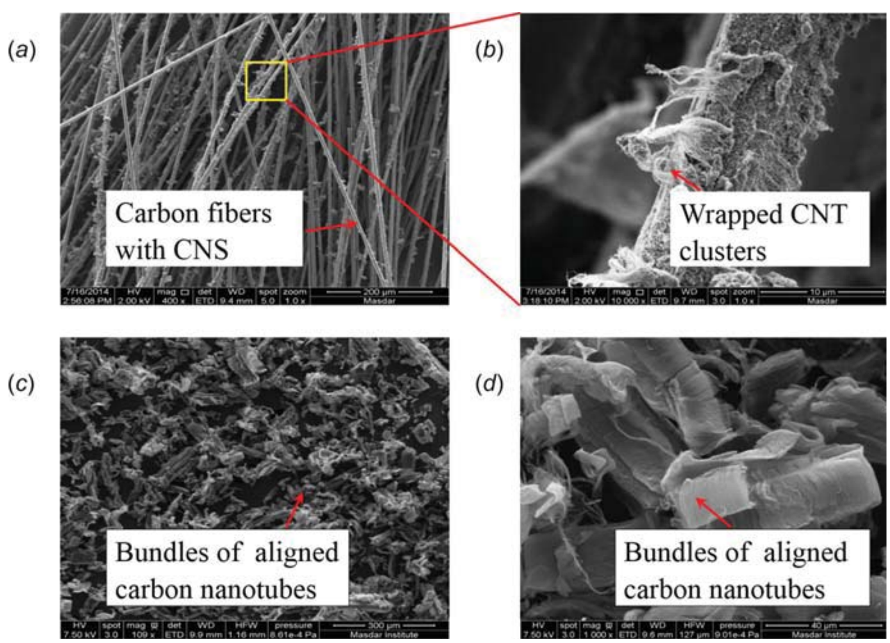

Fig. 2 SEM images: ((*a*) and (*b*)) bundles of aligned CNTs (CNS) grown on glass fiber substrate. ((*c*) and (*d*)) CNS sheared off from the substrate.

Table 1 Geometric parameters of ACSR–Drake transmission wire [25]

Wire name	Stranding (Al/Stl)	Al wire dia. (in.)	Steel wire dia. (in.)	Steel core dia. (in.)	Complete dia. (in.)
Drake	26/7	0.1749	0.136	0.408	1.107

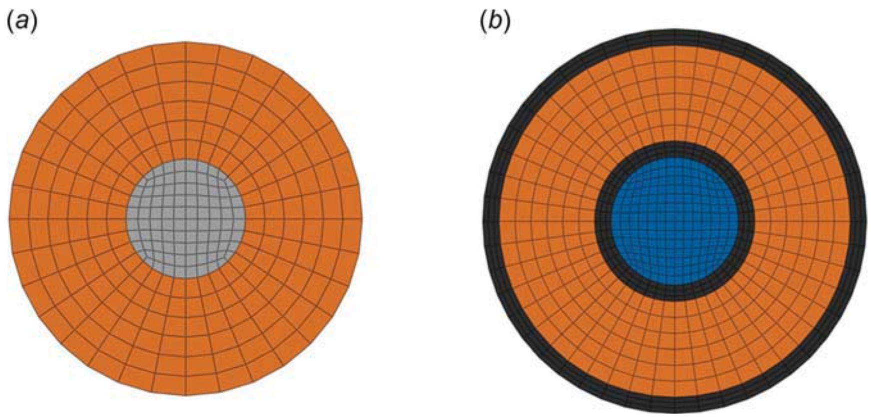

Fig. 3 FE mesh of cross section: (*a*) ACSR line and (*b*) ACCC–CNS line

electrical conductivity of CNS composite layer is measured by van der Pauw method using Lake Shore Cryogenic's integrated Hall effect measurement system. The van der Pauw method is used to determine the electrical resistivity of heterogeneous semiconducting materials using linear four-point probe. In this method, 1 cm $\times$ 1 cm square specimen is cut from the CNS/epoxy composite sheet. In order to facilitate low-resistance electrical connection, four small dots are made with conductive silver paint on four corners of the square sheet. The standard sample mounting card comprising four tungsten needle probes is placed on these four silver dots. The card is then placed in the sample holder and mounted on the Hall effect measurement system to measure the electrical resistivity. The measured electrical conductivity of CNS/epoxy composite is 850–1000 S/m. Uniaxial tensile test was performed to determine the Young's modulus of CNS/epoxy composite. The average Young's modulus of CNS/epoxy is $\sim$3.5 GPa. Thermal conductivity of CNS/epoxy composite is measured using laser flash method, and its average value is $\sim$15 W/m K. CTE of the CNS is in the range of 20–30 $\times$ 10^{-6}/K.

3 Multiphysics Modeling

A coupled analysis of electrical, thermal, and structural fields is necessary for the efficient design of overhead electrical power transmission lines. Heating of the conductor due to its inherent temperature-dependent electrical resistance when it is subjected to electrical potential establishes the link between electrical and thermal fields. Increase in operating temperature of the line increases the conductor's temperature-dependent electrical resistivity which in turn increases the temperature due to Joule heating. On the other hand, the coupling between the thermal and structural fields appears due to temperature-dependent mechanical properties of the line. As the wire temperature increases, the stiffnesses of the core of the line and conductor material decrease leading to increased line sag. The coupling between the electrical and structural fields is due to contact condition change among strands of the line. Air gap between the strands varies with change in contact condition between the strands. Variation in air gap has an influence on the electrical performance of the line. The coupling between the electrical and structural fields is not considered as the stranded cross section of the line is approximated as an equivalent cylindrical cross section as shown in Fig. 1. In FE model for ACSR–Drake wire, Al layer and the core are considered to be perfectly bonded at the interface. Similarly, the interfaces between outer-CNS layer, Al layer, inner-CNS layer, and the core are assumed to be perfectly bonded in FE model of ACCC–CNS wire. In the present study, the multiphysics analysis of power line performance is evaluated using a sequential two-step methodology. In the first step, the coupled electrical–thermal analysis is performed to determine the maximum temperature (operating temperature) of the line for a given current. Using the line operating temperature obtained from the first step, the coupled thermal–structural analysis is carried out in the second step to determine the sag of the ACSR and ACCC–CNS lines.

3.1 Coupled Electrical–Thermal Analysis.

The primary objective of performing coupled electrical–thermal analysis is to determine the temperature rise of overhead transmission line resulting from Joule heating for a given electrical current. Electrical conductivity of the conductor material decreases with increase in temperature which in turn increases the temperature of the line. However, since the overhead power lines are installed in the natural environment, a portion of the heat generated due to Joule heating is dissipated to ambient air in the form of convection and radiation losses. At the same time, the wire absorbs some heat from the sun. The steady-state temperature of the line and the time required to attain such a steady state are determined by the balance between current-induced Joule heating and the heat exchange with the surroundings. Steady-state coupled electrical–thermal FE analysis for ACSR and ACCC–CNS lines was performed using ABAQUS FEA. Line surface temperatures obtained from the FE analysis are benchmarked with those obtained using IEEE Standard 738: 2006 [24]. Table 1 contains the geometric parameters for ACSR–Drake transmission wire used for benchmarking the FE model with IEEE standard. The validated FE model of the ACSR line is then modified to analyze the ACCC–CNS lines.

3.1.1 FE Model. The three-dimensional FE models shown in Fig. 3 are used to perform coupled electrical–thermal analysis with the following approximations:

(1) In alternating current power transmission lines, highest current density occurs at the outermost surface of the conductor, and it reduces toward the core of the line.

Table 2 Transport properties of materials used in FEA [26–31]

Material	Temp. (K)	Electrical conductivity (S/m)	Thermal conductivity (W/(m K))
Aluminum	300	3.54×10^7	237
	400	2.51×10^7	240
	500	1.94×10^7	236
	600	1.58×10^7	231
Steel	300	3.42×10^6	47.2
	400	2.56×10^6	47.8
	500	2.05×10^6	48.1
	600	1.61×10^6	47.2
CNS/epoxy	Ambient	1.0×10^3	15
GFRC	Ambient	1.10×10^{-13}	0.1

Table 3 Thermomechanical properties of materials used in FEA [26–31]

Material	Temp. (K)	Young's modulus (Pa)	Linear coeff. of therm. expansion (10^{-6} K^{-1})
Aluminum	300	7.18×10^{10}	22.3
	400	6.84×10^{10}	23.6
	500	6.33×10^{10}	24.5
	600	5.87×10^{10}	25.5
Steel	300	2.04×10^{11}	10.3
	400	2.01×10^{11}	10.5
	500	1.97×10^{11}	10.7
	600	1.94×10^{11}	10.9
CNS/epoxy	Ambient	3.5×10^9	5.2
GFRC	Ambient	59×10^9	1.6

Therefore, in these FE models, the entire electric current is applied through the outermost nodes of the conductor on one end of wire in the form of nodal current.

(2) Heat generated due to Joule heating in the line dissipates through radiation and convection heat losses. The convective heat loss increases with increase in air velocity. Therefore, natural convection is considered to estimate the convective heat loss, which yields a conservative estimate of conductor surface temperature due to current-induced Joule heating.

The material properties used for FE analysis are given in Tables 2 and 3. In each of these cases, 1 m long wire segment is modeled for coupled thermal–electrical analysis. The electric current is input from one end of the wire through the outer nodes of the conductor in the form of nodal current. Voltage and temperature sink boundary conditions are applied at the other end of the line. The value of film coefficient for natural convection in gases varies between 5 and 10 [32]. (AQ6) The value of film coefficient for natural convection in air is taken equal to 7 and is applied as interaction condition on outer wire surface for both ACCC–CNS and ACSR wires. In the present study, the emissivity of the CNS/epoxy composite at the outer surface of ACCC–CNS wire is taken equal to 0.8 and that of aluminum (oxidized) at outer surface of ACSR wire is taken equal to 0.1. Heat gain from the sun is determined using the procedure outlined in the IEEE Standard 738: 2006 and is applied as heat flux on the outer surface of the line. Its value varies with geography from 850–1350 W/m^2, but a value of 1000 W/m^2 was used in this study. Coupled electrical–thermal eight-noded brick element (DC3D8E) with electrical and thermal degrees-of-freedom is used for thermal–electrical analysis (see Fig. 3). The total number of elements used for the ACSR and ACCC–CNS lines is 5760 and 15,360, respectively. The ACSR and ACCC–CNS wires have different number of layers. In order to maintain the aspect ratio of an average element in each layer the same in both cases, the size of the elements is different, and therefore, the cross section of ACSR and ACCC–CNS wires has different number of elements. The outer surface temperature of the line is determined for a given current from the FE analysis, and the results are compared with the maximum allowable temperature of the line.

3.1.2 Calculating the Conductor Surface Temperature Using IEEE 738: 2006. Per IEEE 738: 2006, the current passing through the line for a given temperature is calculated using the heat balance as given by Eq. (1*b*)

$$q_c + q_r = q_s + I^2 R(T_c) \tag{1a}$$

$$I = \sqrt{\frac{q_c + q_r - q_s}{R(T_c)}} \tag{1b}$$

where q_c is the convection heat loss, q_r is the radiation heat loss, q_s is the heat gain from the sun, I is the current flowing through the line, and $R(T_c)$ is temperature-dependent resistance of the line. Per IEEE standard 738-2006 [24], the heat fluxes (q_c, q_r, and q_s) and wire resistance, R, in Eqs. (1*a*) and (1*b*) are functions of conductor surface temperature. Equation (1*b*) yields the conductor current, I, for given values of heat fluxes (q_c, q_r, and q_s) and wire resistance, R. However, in this problem, we need to calculate the wire surface temperature for a specified value of conductor current. An iterative procedure based on Eq. (1), written in MATLAB, is used to determine the conductor surface temperature. This wire surface temperature obtained from this approach is used to validate the conductor surface temperature obtained from coupled thermal–electrical FE simulation. The conductor surface temperature obtained from FEA simulations is used to perform the parametric study in Sec. 4.3. (AQ7)

3.2 Coupled Thermal–Structural Analysis. In coupled thermal–structural analysis, the main objective is to determine the line sag between two transmission towers. The overall sag in a transmission line is a combination of the following three factors:

(1) self-weight of the transmission line
(2) thermal expansion of the line due to Joule heating
(3) thermal softening of line materials at elevated line operating temperature due to Joule heating

As before, the sag of ACSR–Drake line is considered for verifying the accuracy of the analytical model with the FE model. The validated analytical model is then extended to analyze ACCC–CNS line.

3.2.1 Analytical Model: Sag Calculation by Hybrid Sag Method (HSM). HSM is an improved version of the numerical sag method (NSM) [33]. In NSM, the mechanical load is equally distributed between the core and the conductor, whereas in HSM, the total mechanical load distribution depends upon the stress–strain response of constituent materials of the line. Furthermore, in HSM, the load on the line is initially shared between the core and the conductors, but at a certain operating temperature (knee point), the conductor becomes too soft to an extent of not supporting any load. Beyond this point, the entire load is transferred to the core of the wire leading to bilinear sag behavior (see Fig. 9). Both in HSM and NSM, the initial sag D due to self-weight for a given span length S and initial horizontal tension H applied on the line is described by hyperbolic functions [33]

$$D = \frac{H}{w}\left[\cosh\left(\frac{wS}{2H}\right) - 1\right] \cong \frac{wS^2}{8H} \tag{2}$$

where w is the weight of the line per unit length. The total initial length of the line is given by the following equation:

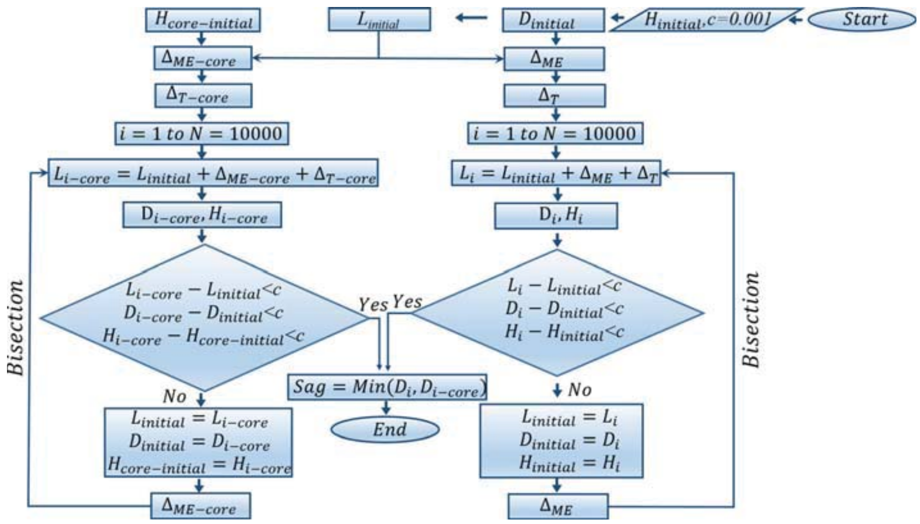

Fig. 4 The flowchart for the sag calculation by HSM

$$L_{\text{initial}} = \frac{2H}{w}\left[\sinh\left(\frac{wS}{2H}\right)\right] \cong S + \frac{8D^2}{3S} \tag{3}$$

The line length increases with increase in temperature due to thermal expansion, and the expression for change in length due to thermal expansion is given by

$$\Delta_T = \alpha_{\text{cond}}(T_{\text{app}} - T_{\text{ref}})\left[L_{\text{initial}}\left(1 - \frac{H_{\text{initial}}}{E_{\text{cond}}A_{\text{cond}}}\right)\right] \tag{4}$$

The change in line length increases the line sag which in turn reduces the stresses in the line. As the tension decreases, the mechanical deformation due to line stresses also decreases, leading to reduced sag. The change in length due to mechanical expansion is calculated using the following equation:

$$\Delta_{\text{ME}} = L_{\text{initial}}\left[\frac{H - H_{\text{initial}}}{E_{\text{cond}}A_{\text{cond}}}\right] \tag{5}$$

Therefore, for a given temperature, final length of the line is the sum of initial length, change in length due to thermal expansion, and change in length due to mechanical elongation as given by Eq. (6). Equations (3)–(6) are applicable to both NSM and HSM. However, Eqs. (5) and (6) are applicable to HSM only

$$L_i = L_{\text{initial}}\left[1 + \left(\frac{H - H_{\text{initial}}}{E_{\text{cond}}A_{\text{cond}}}\right)\right] + L_{\text{initial}}\left[\alpha_{\text{cond}}(T_{\text{app}} - T_{\text{ref}})\left(1 - \frac{H_{\text{initial}}}{E_{\text{cond}}A_{\text{cond}}}\right)\right] \tag{6}$$

The line sag and line tension are recalculated using Eqs. (7*a*) and (7*b*) for this new length of the wire (Eq. (6)), respectively,

$$D_i = \sqrt{\frac{3S(L_i - S)}{8}} \tag{7a}$$

$$H_i = \frac{wS^2}{8D} \tag{7b}$$

In the first iteration, the wire tension H in Eq. (6) is taken as zero. However, in the subsequent iterations, it is replaced by H_i calculated using Eq. (7*b*) per the procedure outlined in Fig. 4 for both ACSR and ACCC–CNS wires.

In the above equations (Eqs. (6) and (7*b*)), H_{initial} is the initial tension applied on the line. The GFRC core consists of epoxy matrix reinforced with continuous microscale S2-glass fibers (60 wt.%) placed in 0deg/90deg directions. Ultimate tensile strength (σ_{UTS}) of these GFRC specimens was found to be 480 MPa through tensile tests. The initial horizontal tension in the wire is calculated considering 15–25% of rated tensile strength as set by the conductor designers. Therefore, assuming that the GFRC core of diameter $d = 10.36$ mm alone sustains the entire load, the initial horizontal tension ($H = (\pi/4)d^2\ 0.2\ \sigma_{\text{UTS}}$) is 8097 N. T_{app} is the instantaneous line operating temperature, and T_{ref} is the reference or ambient temperature. A_{cond} is the total area of the conductor and is determined using the following equations for ACSR and ACCC–CNS lines, respectively:

$$A_{\text{cond}}^{\text{ACSR}} = A_{\text{Al}} + A_{\text{core}} \tag{8a}$$

$$A_{\text{cond}}^{\text{ACCC-CNS}} = A_C + A_{\text{CNS}}^{\text{in}} + A_{\text{Al}} + A_{\text{CNS}}^{\text{out}} \tag{8b}$$

The equivalent Young's moduli of the ACSR and ACCC–CNS lines are given, respectively, by

$$E_{\text{cond}}^{\text{ACSR}} = E_{\text{Al}}\left(\frac{A_{\text{Al}}}{A_{\text{cond}}}\right) + E_{\text{core}}\left(\frac{A_{\text{core}}}{A_{\text{cond}}}\right) \tag{9a}$$

$$E_{cond}^{\text{ACCC-CNS}} = E_C\left(\frac{A_C}{A_{\text{cond}}}\right) + E_{\text{CNS}}^{\text{in}}\left(\frac{A_{\text{CNS}}^{\text{in}}}{A_{\text{cond}}}\right) + E_{\text{Al}}\left(\frac{A_{\text{Al}}}{A_{\text{cond}}}\right) + E_{\text{CNS}}^{\text{out}}\left(\frac{A_{\text{CNS}}^{\text{out}}}{A_{\text{cond}}}\right) \tag{9b}$$

Similarly, the equivalent CTE for the ACSR and the ACCC–CNS lines is given, respectively, by

$$\alpha_{\text{cond}}^{\text{ACSR}} = \alpha_{\text{Al}}\left(\frac{E_{\text{Al}}}{E_{\text{cond}}}\right)\left(\frac{A_{\text{Al}}}{A_{\text{cond}}}\right) + \alpha_{\text{core}}\left(\frac{E_{\text{core}}}{E_{\text{cond}}}\right)\left(\frac{A_{\text{core}}}{A_{\text{cond}}}\right) \tag{10a}$$

$$\alpha_{\text{cond}}^{\text{ACCC-CNS}} = \alpha_C\left(\frac{E_C}{E_{\text{cond}}}\right)\left(\frac{A_C}{A_{\text{cond}}}\right) + \alpha_{\text{CNS}}^{\text{in}}\left(\frac{E_{\text{CNS}}^{\text{in}}}{E_{\text{cond}}}\right)\left(\frac{A_{\text{CNS}}^{\text{in}}}{A_{\text{cond}}}\right) + \alpha_{Al}\left(\frac{E_{\text{Al}}}{E_{\text{cond}}}\right)\left(\frac{A_{\text{Al}}}{A_{\text{cond}}}\right) + \alpha_{\text{CNS}}^{\text{out}}\left(\frac{E_{\text{CNS}}^{\text{out}}}{E_{\text{cond}}}\right)\left(\frac{A_{\text{CNS}}^{\text{out}}}{A_{\text{cond}}}\right) \tag{10b}$$

Table 4 contains the details of the abbreviations used in Eqs. (8)–(10).

Table 4 Abbreviation of terms in Eqs. (8)–(10)

Material	Area	Young's modulus	Linear thermal expansion coefficient
Aluminum	A_{Al}	E_{Al}	α_{Al}
Steel	A_{core}	E_{core}	α_{core}
GFRC	A_C	E_C	α_C
Inner-CNS layer	A_{CNS}^{in}	E_{CNS}^{in}	α_{CNS}^{in}
Outer-CNS layer	A_{CNS}^{out}	E_{CNS}^{out}	α_{CNS}^{out}

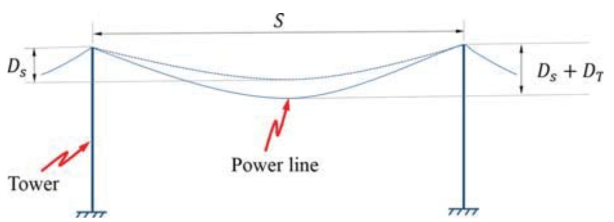

Fig. 5 Sag of the line between supporting towers

Since the line sag, line length, and line tension are implicitly connected to each other, an iterative procedure shown in Fig. 4 is employed to determine their converged values.

3.2.2 Line Sag Calculation Using FEA. A two-dimensional FE beam model is used for line sag calculations (see Fig. 5). The structural B31 element type (two-node linear beam in space) is used for the FE model of both types of transmission lines. The FE model consists of 5486 beam elements along the span length. The equivalent material properties required for FEA are calculated using the formulas given in the previous section. Thermomechanical FE analysis was performed considering geometric nonlinear effects in two steps. In the first step, the sag due the self-weight of the line is determined. In the second step, the simultaneous effect of both self-weight and the sag due to thermal expansion is determined. Therefore, the total line sag is given by

$$D = D_s + D_T \tag{11}$$

where D_s and D_T are line sag due to self-weight and thermal expansion of the line, respectively. The densities of the Al conductors, CNS, glass fiber, and steel are 2765.87 kg/m^3, 1500 kg/m^3, 1500 kg/m^3, and 7850 kg/m^3, respectively. The connections between consecutive supporting towers and the line at both the ends are treated as encastred boundary condition. Initial and final temperatures of the line are specified using temperature boundary conditions on the entire line in the initial and subsequent steps, respectively.

4 Results and Discussion

4.1 Coupled Electrical–Thermal Analysis. Figure 6 shows the steady-state surface temperature of the line obtained from the FEA and IEEE standard for the ACSR–Drake wire as a function of transmitted electric current. The operating temperature of the line increases with increase in input current, and the results obtained from these two approaches are in good agreement (see Fig. 6). The validated FE model is then extended to analyze ACCC–CNS line. Figure 7 shows the comparison of line surface temperature as a function of electric current for ACSR–Drake and equivalent ACCC–CNS wires. Figure 7 reports that the operating temperature of the ACCC–CNS line is lower than that of an equivalent ACSR line over the entire range of operating electric current. For a given input current (907 A), ACSR line reaches a steady-state temperature of 87 °C whereas the steady-state

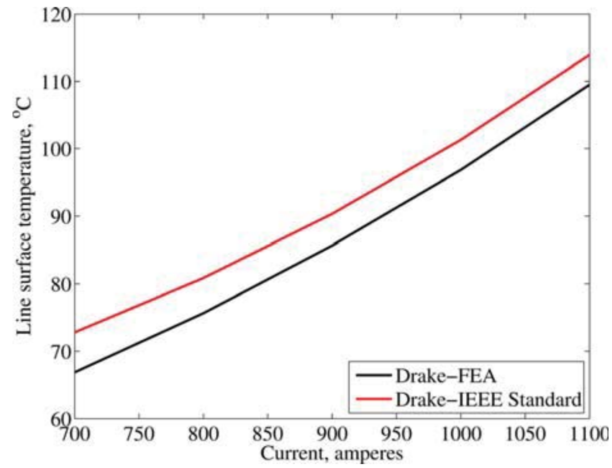

Fig. 6 Comparison of surface temperature for ACSR–Drake transmission line as a function of the current: IEEE standard versus FEA

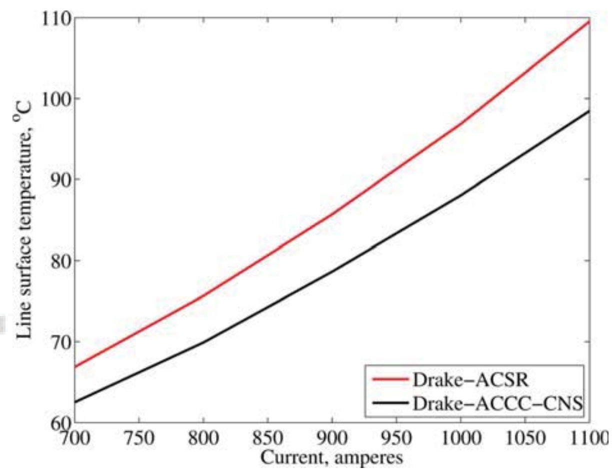

Fig. 7 Comparison of surface temperature of ACCC–CNS line with its equivalent ACSR line obtained from FEA as a function of the current

operating temperature for an equivalent ACCC–CNS wire is 78 °C. Reduced operating temperature of ACCC–CNS line reduces the line losses and line sag due to temperature dependence of electrical conductivity and stiffness, respectively. Figure 8 shows the temperature distribution across the cross section of the line at different time intervals obtained from transient coupled thermal–electrical FEA performed for ACSR and ACCC–CNS lines, respectively. As observed in Fig. 8(*a*), the ACSR line attains a uniform temperature in 18.70 s whereas ACCC–CNS line attains a uniform temperature in 1006 s as shown in Fig. 8(*b*). Due to low thermal conductivity of the core and high emissivity of the outer layer, the time to attain thermal equilibrium for ACCC–CNS line is much higher than that of an equivalent ACSR wire. This is very helpful in protecting the integrity of the wire in the event of sudden increase in current for a short period as in case of a short circuit.

4.2 Coupled Thermal–Structural FE Analysis. Figure 9 shows the comparison of line sag determined using NSM, HSM, and FEA as a function of line operating temperature. The results of both NSM and HSM are in good agreement with those obtained from FEA. Figure 10 shows the contour plot of the sag obtained from FEA for the ACSR–Drake line. According to the studies

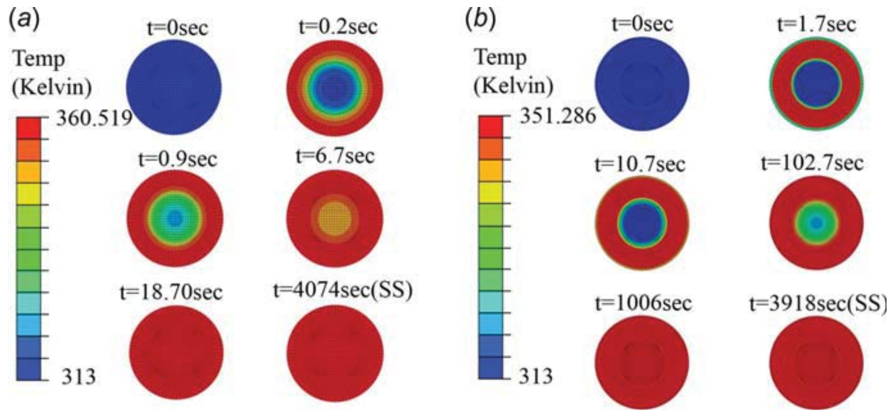

Fig. 8 Temperature (Kelvin) contour plots of the line at different time intervals from transient coupled thermal–electrical analysis of (*a*) ACSR–Drake line and (*b*) ACCC–CNS line

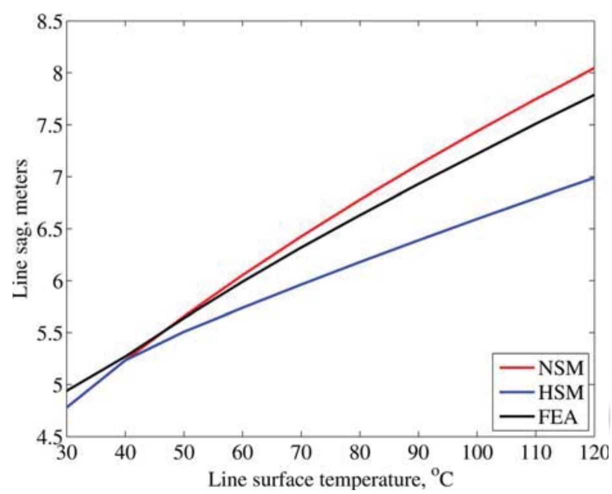

Fig. 9 Sag for ACSR–Drake line at different operating temperatures obtained using NSM, HSM, and FEM

carried out by the Southwire Company, the sag in high-capacity wires exhibits a bilinear behavior [34]. At low temperature, the wire sag is controlled by both core and conductor. However, at elevated temperatures, the sag behavior of the wire is governed by the thermomechanical properties of the core. The HSM correctly accounts for this bilinear behavior by differentiating the sag behavior above and below the knee point. In case of FEA, the equivalent properties (especially equivalent coefficient of thermal expansion) of the wire of B31 beam elements are calculated using rule of mixture of composite materials for the entire range of wire operating temperature, and therefore, HSM tends to overestimate the thermal response at elevated temperatures. However, FEA results are more conservative than those obtained from HSM but do not capture the bilinear sag behavior. Moreover, FEA requires more computational effort than the analytical method. Therefore, HSM is employed to perform parametric study of the ACCC–CNS wire. Figure 11 compares the line sag for ACSR and the equivalent ACCC–CNS line determined using HSM as a function of temperature. It is clear from Fig. 11 that the ACCC–CNS line sags less than that of its equivalent ACSR line over the entire range of operating temperature.

4.3 Parametric Study. The primary objective of this parametric study is to identify an optimal set of design parameters for the ACCC–CNS line by performing sequentially coupled electrical–thermal and thermal–structural analyses. An iterative procedure outlined in Fig. 12 is employed to perform these parametric studies. Geometric parameters (core diameter and span length) of ACCC–CNS line and input current are considered as primary inputs. A MATLAB code was developed and used in conjunction with HSM to perform these parametric studies by incrementally varying the input parameters. The temperature of the line obtained from the coupled electrical–thermal analysis serves as an input to coupled thermal–structural analysis (sag calculation) and vice versa. The geometric parameters of ACCC–CNS line are optimized by comparing its performance with that of an equivalent ACSR line for a given current. Figure 7 shows that the operating temperature of the ACCC–CNS line is 78 °C for 907 A whereas the operating temperature of the ACSR line for the same current is 87 °C. Similarly, Fig. 11 shows that the line sag for ACSR and ACCC–CNS lines is equal to 6.3 m and 4.2 m at their

Fig. 10 Displacement contour plot of ACSR–Drake line representing the sag between two transmission towers obtained from FEA

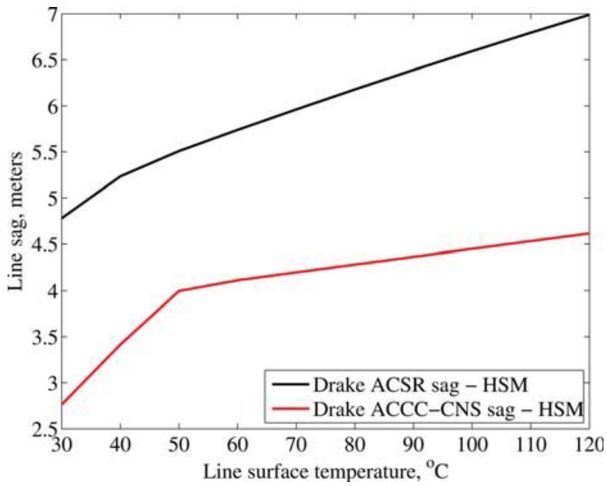

Fig. 11 Sag for ACCC–CNS line and its equivalent ACSR line as a function of operating temperature by HSM

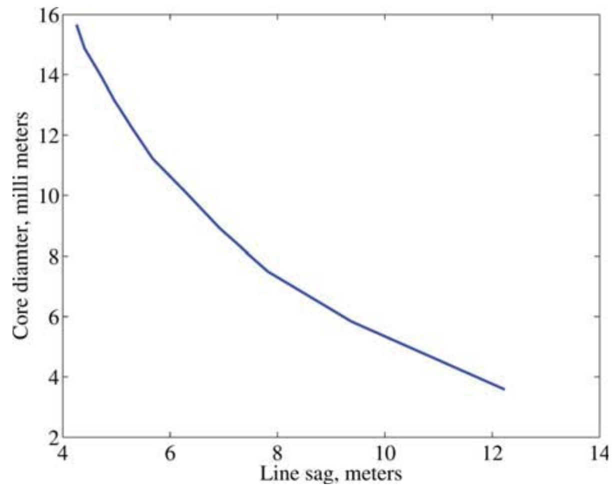

Fig. 13 ACCC–CNS line sag variation as a function of the core diameter of the line operating at its CCC of each configuration for given span length

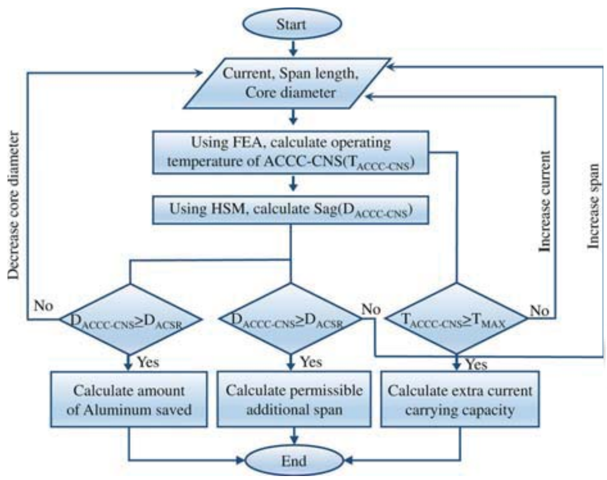

Fig. 12 The flowchart for parametric study

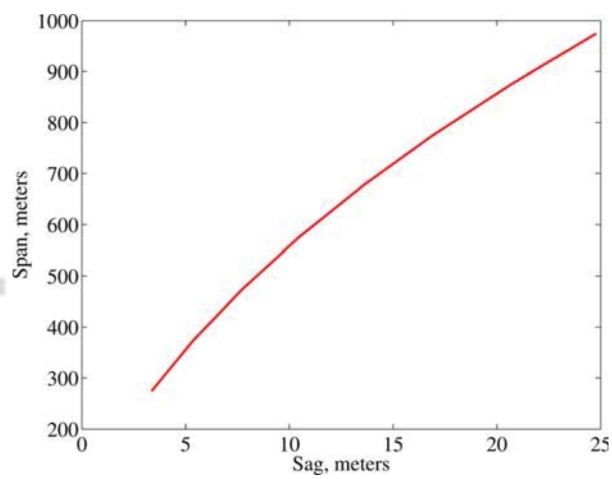

Fig. 14 ACCC–CNS line sag variation with respect to span length for a given core diameter

respective operating temperatures for the same input current (907 A), respectively. These results show that the ACCC–CNS line has less line losses and lower sag compared to those of an equivalent ACSR line. This motivates to further optimize the performance of ACCC–CNS line considering ACSR line's performance as a baseline for a given input current. Therefore, span length between two supports and the core diameter are chosen as parameters for line sag comparison, and the input current is chosen as a parameter for line temperature comparison. In all cases, the outer diameter of the wire remains unchanged to maintain the constant size of the wire as the core diameter is varied.

One of the optimal configurations of the ACCC–CNS line is obtained by varying the core diameter of the line and comparing ACCC–CNS line sag with ACSR line sag for a given span length (274.3 m) and current (907 A). From Fig. 13, it can be seen that the ACCC–CNS line of core diameter ~11 mm experiences the same sag as that of ACSR line. It indicates that the ACCC–CNS line can accommodate around 25 vol. % more aluminum than its equivalent ACSR line. Similarly, another optimal configuration of ACCC–CNS line is obtained by varying the span length and comparing the ACCC–CNS line sag with ACSR line sag for a given core diameter (14.05 mm) and current (907 A). Figure 14 shows that the span length $S = 355$ m produces the same sag as that of ACSR line with $S = 274.3$ m. It is therefore clear from Fig. 14 that the new ACCC–CNS line can accommodate more span length

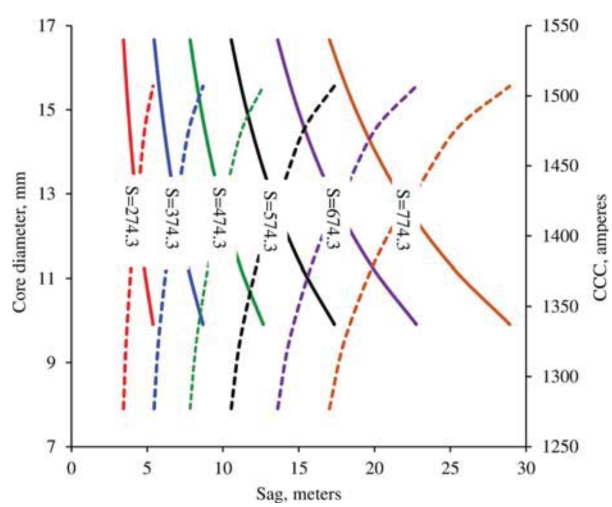

Fig. 15 Optimal performance map: ACCC–CNS line sag and CCC for different core diameters and span lengths

compared to the ACSR line. Furthermore, to generate an optimal design map for the ACCC–CNS line, the input current is varied until the operating temperature of ACCC–CNS line reaches the maximum allowable temperature (assumed 120 °C). Results indicate that the ACCC–CNS line can carry additional 370 A of current with the same amount of aluminum as in ACSR line. In addition, the sag and CCC are calculated for different configurations by varying the span length and core diameter of the ACCC–CNS line. Figure 15 shows the sag and the CCC values for different configurations (span lengths and core diameter) of the ACCC–CNS line at maximum operating temperature. Solid lines indicate the core diameter versus sag, and the dotted lines indicate CCC versus sag for different span lengths. This optimal performance map can be used as a tool to design high-performance transmission lines.

5 Conclusion

A novel design alternative to existing ACSR line, comprising CNS coating in a multilayered architecture (ACCC–CNS), is proposed and its ampacity and sag performance are evaluated. Extensive characterization and experimental tests were conducted to evaluate electrothermal and thermomechanical properties of CNS material and CNS/epoxy composites. Coupled field analyses based both on computational and analytical methods are presented. The results of both analytical and computational models indicate that the ACCC–CNS line has superior performance compared to that of the ACSR line in terms of reduced operating temperature, CCC, and line sag. Furthermore, the parametric studies were performed for the ACCC–CNS line by varying the geometric parameters and input current. Results of the parametric studies were compared with those of ACSR line to estimate the percentage of reduction in core diameter and percentage of increase in span length. A design optimization study conducted to construct an optimum performance map indicates that by replacing the ACSR line by an ACCC–CNS line, we could save about 25 vol. % of aluminum, increase permissible span length by 80 m, and increase the CCC by 370 A, for the parameters used herein. The findings of this study indicate that the use of CNS material in conjunction with GFRC improves the transmission efficiency of lines due to reduced operating temperature and sag, leading to reduced CO_2 emissions.

Acknowledgment

This work was supported by Lockheed Martin Corporation (Project code: EX2014-000027). The authors would like to thank Ms. Maribeth Malloy, Mr. Sunil Pancholi, and Mr. Scott Stallard of Lockheed Martin Corporation, USA, for their constructive suggestions and helpful hints.

References

[1] Pal, G., and Kumar, S., 2016, "Modeling of Carbon Nanotubes and Carbon Nanotube–Polymer Composites," Prog. Aerosp. Sci., **80**, pp. 33–58.

AQ14 [2] Pal, G., and Kumar, S., 2016, "Multiscale Modeling of Effective Electrical Conductivity of Short Carbon Fiber-Carbon Nanotube-Polymer Matrix Hybrid Composites," Mater. Des., **89**, pp. 129–136.

[3] Arif, M. F., Kumar, S., and Shah, T., 2016, "Tunable Morphology and Its Influence on Electrical, Thermal and Mechanical Properties of Carbon Nanostructure-Buckypaper," Mater. Des., **101**, pp. 236–244.

AQ9 [4] Adams, H., and Reynolds Metals Co, 1974, "Steel Supported Aluminum Overhead Conductors," U.S. Patent No. 3,813,481.

[5] Deve, H., and Anderson, T., 2003, "3M Aluminum Conductor Composite Reinforced Technical Notebook (795 kcmil Family): Conductor and Accessory Testing," 3M, St. Paul, MN.

AQ10 [6] ■, 2011, *Engineering Transmission Lines With ACCC Conductor*, 1st ed., CTC Global, ■.

[7] Alawar, A., Bosze, E. J., and Nutt, S. R., 2005, "A Composite Core Conductor for Low Sag at High Temperatures," IEEE Trans. Power Delivery, **20**(3), pp. 2193–2199.

[8] Burks, B., Armentrout, D. L., and Kumosa, M., 2010, "Failure Prediction Analysis of an ACCC Conductor Subjected to Thermal and Mechanical Stresses," IEEE Trans. Dielectr. Electr. Insul., **17**(2), pp. 588–596.

[9] Burks, B., Armentrout, D., and Kumosa, M., 2011, "Characterization of the Fatigue Properties of a Hybrid Composite Utilized in High Voltage Electric Transmission," Composites, Part A, **42**(9), pp. 1138–1147.

[10] Burks, B., Middleton, J., and Kumosa, M., 2012, "Micromechanics Modeling of Fatigue Failure Mechanisms in a Hybrid Polymer Matrix Composite," Compos. Sci. Technol., **72**(15), pp. 1863–1869.

[11] Hoffman, J., Middleton, J., and Kumosa, M., 2015, "Effect of a Surface Coating on Flexural Performance of Thermally Aged Hybrid Glass/Carbon Epoxy Composite Rods," Compos. Sci. Technol., **106**, pp. 141–148. AQ15

[12] Kocar, I., and Ertas, A., 2004, "Thermal Analysis for Determination of Current Carrying Capacity of PE and XLPE Insulated Power Cables Using Finite Element Method," 12th IEEE Mediterranean Electrotechnical Conference, MELECON 2004, Dubrovnik, Croatia, May 12–15, Vol. 3, pp. 905–908.

[13] Karahan, M., and Kalenderli, O., 2011, "Coupled Electrical and Thermal Analysis of Power Cables Using Finite Element Method," *Heat Transfer—Engineering Applications*, V. S. Vikhrenko, ed., InTech, ■, pp. 205–230. AQ11

[14] Hwang, C. C., and Jiang, Y. H., 2003, "Extensions to the Finite Element Method for Thermal Analysis of Underground Cable Systems," Electr. Power Syst. Res., **64**(2), pp. 159–164.

[15] Nguyen, N., Vu, P., and Tlusty, J., 2010, "New Approach of Thermal Field and Ampacity of Underground Cables Using Adaptive hp-FEM," IEEE PES T&D 2010, New Orleans, LA, Apr. 19–22, pp. 1–5.

[16] Mensah-Bonsu, C., Krekeler, U. F., Heydt, G. T., Hoverson, Y., Schilleci, J., and Agrawal, B. L., 2002, "Application of the Global Positioning System to the Measurement of Overhead Power Transmission Conductor Sag," IEEE Trans. Power Delivery, **17**(1), pp. 273–278.

[17] Keshavarzian, M., and Priebe, C. H., 2000, "Sag and Tension Calculations for Overhead Transmission Lines at High Temperatures-Modified Ruling Span Method," IEEE Trans. Power Delivery, **15**(2), pp. 777–783.

[18] de Villiers, W., Cloete, J. H., Wedepohl, L. M., and Burger, A., 2008, "Real-Time Sag Monitoring System for High-Voltage Overhead Transmission Lines Based on Power-Line Carrier Signal Behavior," IEEE Trans. Power Delivery, **23**(1), pp. 389–395.

[19] Albizu, I., Mazon, A. J., and Zamora, I., 2009, "Flexible Strain-Tension Calculation Method for Gap-Type Overhead Conductors," IEEE Trans. Power Delivery, **24**(3), pp. 1529–1537.

[20] Du, Y., and Liao, Y., 2011, "Online Estimation of Power Transmission Line Parameters, Temperature and Sag," North American Power Symposium (NAPS), Boston, MA, Aug. 4–6, pp. 1–6.

[21] Shah, T. K., Gardner, S. H., Alberding, M. R., and Applied Nanostructured Solutions, LLC, 2012, "CNT-Infused Fiber and Method Therefor," U.S. Patent No. 8,158,217.

[22] Malet, B. K., Shah, T. K., and Applied Nanostructured Solutions, LLC, 2014, "Glass Substrates Having Carbon Nanotubes Grown Thereon and Methods for Production Thereof," U.S. Patent No. 8,784,937.

[23] Shah, T. K., Malecki, H. C., Adcock, D. J., and Applied Nanostructured Solutions, LLC, 2014, "CNT-Based Resistive Heating for Deicing Composite Structures," U.S. Patent No. 8,664,573.

[24] IEEE, 2006, "IEEE Standard for Calculating the Current-Temperature of Bare Overhead Conductors," IEEE, Piscataway, NJ, Standard No. 738-2006.

[25] Southwire, ■, "ACSR: Aluminum Conductor Steel Reinforced Bare, 11-4ACSR," Southwire Company, LLC, Carrollton, GA. AQ12

[26] Henry, S. D., Frueh, S. E., Boring, R., Levicki, D., and Harrision, L., 1993, *ASM Specialty Handbook, Aluminum and Aluminum Alloys*, ASM International, Materials Park, OH, pp. 658–662.

[27] Aluminum Association, 1971, *Aluminum Electrical Conductor Handbook*, The Aluminum Association, Arlington, VA.

[28] Gandy, D., 2007, *Carbon Steel Handbook*, Electric Power Research Institute, Palo Alto, CA.

[29] Spitalsky, Z., Tasis, D., Papagelis, K., and Galiotis, C., 2010, "Carbon Nanotube–Polymer Composites: Chemistry, Processing, Mechanical and Electrical Properties," Prog. Polym. Sci., **35**(3), pp. 357–401.

[30] Hartman, D. R., Greenwood, M. E., and Miller, D. M., 1994, "High Strength Glass Fibers," 39th International SAMPE Symposium and Exhibition: Moving Forward With 50 Years of Leadership in Advanced Materials, Anaheim, CA, Apr. 11–14, Vol. 39, pp. 521–533.

[31] Vilatela, J. J., Khare, R., and Windle, A. H., 2012, "The Hierarchical Structure and Properties of Multifunctional Carbon Nanotube Fibre Composites," Carbon, **50**(3), pp. 1227–1234.

[32] ■, 2015, "■," Colorado State University, Fort Collins, CO. AQ13

[33] Alawar, A., Bosze, E. J., and Nutt, S. R., 2006, "A Hybrid Numerical Method to Calculate the Sag of Composite Conductors," Electr. Power Syst. Res., **76**(5), pp. 389–394.

[34] Thrash, R., Hudson, G., Cooper, D., and Sanders, G., 1994, *Overhead Conductor Manual*, 1st ed., Southwire Company, Carrollton, GA.